

JGR Space Physics

RESEARCH ARTICLE

10.1029/2023JA032050

Key Points:

- A hybrid model qualitatively reproduced the vertical potential drop and field aligned currents in Martian crustal magnetic cusp regions
- The vertical electric potential drop is mostly from the Hall electric field as a result of energy input from the downward plasma flow
- The vertical electric potential drop decreases with ionospheric ion density and increases with magnetic field strength

Correspondence to:

Y. Dong,
yaxue.dong@lasp.colorado.edu

Citation:


Dong, Y., Brain, D. A., Jarvinen, R., & Poppe, A. R. (2024). Localized hybrid simulation of Martian crustal magnetic cusp regions: Vertical electric potential drop and plasma dynamics. *Journal of Geophysical Research: Space Physics*, 129, e2023JA032050. <https://doi.org/10.1029/2023JA032050>

Received 4 SEP 2023
Accepted 8 JAN 2024

Author Contributions:

Conceptualization: David A. Brain
Formal analysis: Yaxue Dong
Funding acquisition: David A. Brain
Investigation: Yaxue Dong
Methodology: Yaxue Dong, David A. Brain, Riku Jarvinen, Andrew R. Poppe
Project administration: David A. Brain
Resources: David A. Brain, Riku Jarvinen
Software: Yaxue Dong, Riku Jarvinen
Supervision: David A. Brain
Validation: Yaxue Dong, Riku Jarvinen, Andrew R. Poppe
Visualization: Yaxue Dong
Writing – original draft: Yaxue Dong
Writing – review & editing: David A. Brain, Riku Jarvinen, Andrew R. Poppe

Localized Hybrid Simulation of Martian Crustal Magnetic Cusp Regions: Vertical Electric Potential Drop and Plasma Dynamics

Yaxue Dong¹ , David A. Brain¹ , Riku Jarvinen² , and Andrew R. Poppe³ 

¹Laboratory for Atmospheric and Space Physics, University of Colorado, Boulder, CO, USA, ²Finnish Meteorological Institute, Helsinki, Finland, ³Space Sciences Lab, University of California, Berkeley, CA, USA

Abstract The localized crustal magnetic fields of Mars play an important role in the planet's ionosphere-solar wind interaction. Various physical processes in the induced magnetosphere, such as particle precipitation, field-aligned currents, and ion outflow, are usually associated with the crustal magnetic cusp regions, where field lines are mostly vertical and open to space. Due to the small spatial scale (a few hundred km) of the Martian crustal magnetic cusps, localized models with high spatial resolutions and ion kinetics are needed to understand the physical processes. We adapt the simulation platform HYB developed at the Finnish Meteorological Institute to a moderately strong magnetic cusp above the Martian exobase with a 2-D simulation domain assuming periodic boundary conditions on the third dimension. Two plasma sources are included in the simulation: hot protons from the induced magnetosphere and cold heavy ions (O^+) from the ionosphere. Our model results can qualitatively reproduce the vertical electric potential drop, particle transport, and field aligned current in the cusp region. The vertical electric potential is built up mostly by the Hall electric field as a result of the separation between ion and electron fluxes of the downward plasma flow. By varying the model inputs, we found that the vertical potential drop depends on ionospheric ion density and magnetic field strength. These results tell us that energy is transferred from magnetospheric plasma to ionospheric plasma through the vertical electric potential buildup in magnetic cusps and how this process may affect electron precipitation, ion escape, and ionosphere conditions at Mars.

1. Introduction

Mars' global dipole magnetic field shut down long ago at a very early age (e.g., Mittelholz et al., 2020), with only localized patches of remnant magnetism in the crust also known as crustal fields. The first global map of the crustal fields of Mars was established based on Mars Global Surveyor (MGS) data (Acuña et al., 1998, 1999), which showed highly variable spatial distributions near the surface with the field strength up to $\sim 1,500$ nT. These crustal fields play an important role regarding solar wind-ionosphere interactions resulting in both local and global effects on the plasma environment of Mars, such as modifying draped interplanetary magnetic field (IMF) around the planet (e.g., Brain et al., 2003; Dong et al., 2019; Harada et al., 2018; Kallio et al., 2008), shaping the ionosphere (e.g., Andrews et al., 2015; Dubinin et al., 2016; Mitchell et al., 2001), diverting ion flows (e.g., Fan et al., 2020; Li et al., 2022), influencing plasma boundaries (e.g., Brain et al., 2005; Edberg et al., 2008; Fang et al., 2017), and affecting ion escape (e.g., Brain et al., 2010; Brecht & Ledvina, 2014; Fang et al., 2015; Nilsson et al., 2011; Ramstad et al., 2016; Weber et al., 2021). It is well known that the polar cusps of the Earth's magnetosphere, where shocked solar wind in the magnetosheath can access ionosphere directly usually thought to be through magnetic reconnections, play an important role in the ionosphere-magnetosphere coupling (Smith & Lockwood, 1996 and references therein). These regions are associated with a number of geophysical phenomena, such as field-aligned currents, ion outflow, and aurorae (Axford, 1968; Heikkila & Winningham, 1971; Iijima & Potemra, 1976). At Mars, the regions where the magnetic field lines are mostly vertical and open from the surface through the ionosphere to space are called crustal magnetic cusps by analogy to Earth. Similarly, various interesting physical processes take place in Martian crustal magnetic cusps, including aurorae, field-aligned currents, electron precipitation, and cold ion outflow (see Brain & Halekas, 2012; Dubinin et al., 2008; Leblanc et al., 2006; Lundin et al., 2006; Xu et al., 2014), which are all related to the electric potential structure in the magnetic cusp regions.

Ion escape is an important atmospheric loss process of Mars (Jakosky et al., 2018 and references therein). Numerous previous studies based on the data from the ESA Mars Express (MEX) (Chicarro et al., 2004) and

NASA Mars Atmosphere and Volatile Evolution (MAVEN) (Jakosky et al., 2015) missions have revealed that low energy ions dominate the total ion escape rates at Mars (e.g., Dong et al., 2023; Nilsson et al., 2011; Ramstad et al., 2015). Cold ion outflow through crustal magnetic cusps may contribute significantly to these low energy escaping ions (Inui et al., 2018). Different types of aurorae have been observed at Mars by MEX, MAVEN, and the Emirates Mars Mission (Bertaux et al., 2005; Chaffin et al., 2022; Deighan et al., 2018; Leblanc et al., 2008; Ritter et al., 2018; Schneider et al., 2015), among which the discrete aurora is considered to be caused by energetic electrons precipitating through magnetic cusps (Brain et al., 2006; Gérard et al., 2015; Leblanc et al., 2006; Schneider et al., 2021). Although both ion and electron accelerations associated with Martian magnetic cusps or open field lines have been observed by MGS, MEX, and MAVEN (e.g., Dubinin et al., 2009; Halekas et al., 2008; Xu et al., 2020), the mechanisms leading to such accelerations are not clear yet. Studying the electric potential buildup and plasma dynamics in the crustal magnetic cusp region is important for better understanding Martian atmospheric loss and aurorae.

There have been some simulation works regarding the role of crustal fields in the plasma environment of Mars. The global effects of crustal fields on the Martian induced magnetosphere and ion escape have been discussed based on magnetohydrodynamic (MHD) and hybrid models (e.g., Brecht & Ledvina, 2014; Fang et al., 2015, 2017; Kallio et al., 2008; Ma et al., 2002; Ma et al., 2014). Furthermore, Ma et al. (2018) applied Hall-MHD embedded with particle-in-cell (PIC) simulations to study the reconnection between crustal field and nightside draped field and the effects on magnetotail dynamics. Rioussat et al. (2013, 2014) simulated the electric currents, fields, and plasma dynamics in the dynamo region near crustal fields using a multi-fluid model. In Li et al. (2022)'s multifluid MHD model, it is shown that the ionospheric heavy ion flow is deflected by crustal fields. However, there are very few localized simulation models with kinetic effects focusing on the magnetic cusp regions. Poppe et al. (2021) developed a 1.5 dimensional (one spatial dimension the along magnetic field line and two velocity dimensions parallel and perpendicular to the magnetic field) PIC model, which showed the field-aligned electric potential drop can be up to tens of volts. In this paper, we will present our 2-D hybrid simulation model of Martian crustal magnetic cusp regions, compare our results with other localized simulation models, and discuss how these results are related to Martian ionosphere conditions, ion loss, and aurorae.

2. Model Description and Setup

The HYB hybrid code has been successfully applied to both global and localized simulations of planetary plasma environments (e.g., Jarvinen et al., 2014; Jarvinen et al., 2010; Kallio et al., 2008; Kallio et al., 2010). As shown by the following equations, the hybrid simulation model tracks ions as individual particles moving under electromagnetic fields (Equation 1), treats electrons as a massless neutralizing fluid (Equations 2 and 3), and calculates electric current density and electromagnetic fields based on Ampere's law, generalized Ohm's law, and Faraday's law (Equations 4–6).

$$m_i d\mathbf{v}_i/dt = e(\mathbf{E} + \mathbf{v}_i \times \mathbf{B}) \quad (1)$$

$$n_e = n_i \quad (2)$$

$$\mathbf{U}_e = \mathbf{U}_i - \mathbf{J}/(n_e e) \quad (3)$$

$$\mathbf{J} = \nabla \times \mathbf{B}/\mu_0 \quad (4)$$

$$\mathbf{E} = -\mathbf{U}_i \times \mathbf{B} + \mathbf{J} \times \mathbf{B}/(n_e e) - \nabla P_e/(n_e e) \quad (5)$$

$$\partial \mathbf{B}/\partial t = -\nabla \times \mathbf{E} \quad (6)$$

In the equations above, m_i and \mathbf{v}_i are the mass and velocity of an individual ion; \mathbf{J} is the electric current density; \mathbf{E} and \mathbf{B} are the electric and magnetic fields; n_i and \mathbf{U}_i are the ion density and bulk velocity; n_e , \mathbf{U}_e , and P_e are the electron density, flow velocity, and pressure; e is the positive elementary charge; and μ_0 is the magnetic vacuum permeability. The ion density and bulk velocity are obtained from the spatial and velocity distributions of individual ions in each cube shaped and constant-sized grid cell. The three terms in Equation 5 are convection electric field, Hall electric field, and ambipolar electric field, respectively. Since these model runs use an assumption of isothermal electron fluid, the third term (the electron pressure term) is only a rough estimate of the

Table 1
Model Setting

Box size ^a ($x \times y$)	$[0, 200] \times [-200, 200]$ (km)
Spatial resolution	5 km
Time step	0.1 ms
Magnetic field strength	100 nT
Magnetospheric plasma	H ⁺
H ⁺ density	1 cm ⁻³
H ⁺ flow velocity	100 km/s
H ⁺ temperature	25 eV
Ionospheric plasma	O ⁺
O ⁺ density	10 cm ⁻³
O ⁺ flow velocity	1 km/s
O ⁺ temperature	1 eV

^aThis is smaller than the simulation domain to avoid artificial boundary effects. See Section 2.

ambipolar electric field with a manually set constant ionosphere electron temperature $T_e = 2,000$ K based on MAVEN measurements of the electron temperature at the altitudes of ~ 200 – 400 km (Ergun et al., 2021) ($P_e = n_e k T_e$). Other terms in the full generalized Ohm's law, such as electron inertia, are not included in these model runs. The resistivity term ($\eta_a \mathbf{J}$) is only included in the evolution of magnetic field calculated with Equation 6 to add explicit magnetic diffusion (e.g., Jarvinen et al., 2018). The manually selected value for anomalous resistivity ($\eta_a \approx 6,000 \Omega\text{m}$) allows magnetic field to diffuse on time scales much longer than the simulation time step.

We apply this model to a portion of a moderately strong magnetic cusp above the exobase (lower boundary), mimicked by a magnetic dipole under the lower boundary aligned with the vertical axis (x axis) with a maximum field strength of 100 nT at the lower boundary ($x = 0$). Since the magnetic configuration is symmetric with the vertical axis, we use a 2-D simulation domain with periodic boundary conditions in the third dimension for efficiency. Theoretically, this 2-D simulation domain is equivalent to a 3-D domain with infinite distance in the third dimension instead of a cylindrically symmetric configuration. We will further discuss the effect of this setting in Section 4. The simulation domain is set to be 600–400 km in the

vertical (x) and horizontal (y) directions respectively. In order to avoid any artificial boundary effects, we only analyze the model results within a smaller box of 400–200 km. Two plasma source populations are included: a hot, fast, and tenuous magnetospheric plasma flow represented by protons injected from the upper boundary and a cold, slow, and dense ionospheric plasma flow represented by oxygen ions injected from the lower boundary. All the model setting parameters are shown in Table 1. The time step Δt and spatial resolution Δx in Table 1 generally meets the Courant–Friedrichs–Lewy condition considering the whistler wave mode in such hybrid simulation: $\Delta t \leq \Delta x^2 \mu_0 n_e e / (2\pi B)$ (see Alho, 2016 for details) with the electron density $n_e \sim$ a few cm⁻³ and magnetic field $B \sim$ tens of nT (see Figures 2 and 3). The inertial lengths ($d_i = \sqrt{m_i / (\mu_0 n_i e^2)}$) for H⁺ and O⁺ are ~ 200 and ~ 500 km respectively with the ion density (n_i) of the two ion species to be ~ 1 – 2 and ~ 2 – 5 cm⁻³ respectively (see Figure 3). The inertial lengths for both ion species are comparable to the spatial scale of the simulation domain, which tells us that the ion kinetic effects are significant in such magnetic cusp regions (Tóth et al., 2017). The gyroperiods ($T = 2\pi m_i / (eB)$) for H⁺ and O⁺ are ≥ 0.65 and ≥ 10 s respectively with $B \leq 100$ nT. The time step in Table 1 is much smaller than both H⁺ and O⁺ gyroperiods, which is valid for the study of ion kinetics. Since the ions are tracked as individual particles in this model, the ion gyroradius is not directly related to the choice of the spatial resolution. We will discuss the effects of ion gyroradii on the model results in Section 3. Gravity is not included in the model runs, the effects of which will be discussed in Sections 3 and 5.

3. Model Results

We run the model until it converges to a steady state. As shown in Figure 1, the injection and escape rates stay approximately equal to each other for both ion species after ~ 50 s of simulation time. Since gravity is not included in the model run, almost all injected planetary O⁺ ions from the lower boundary are expected to leave the simulation domain through the upper boundary with an escape rate matching the injection rate when the model converges. The purpose of this work is not to model ion escape rates, but to model the ion dynamics and electric potential structures in the crustal magnetic cusp regions. The spike in the vertical electric potential drops at ~ 85 s as shown in Figure 1b is likely to be a statistical noise, which was eventually stabilized as the model continued running and should not affect any model results after. After ~ 100 s, the vertical electric potential drops at different locations along the upper boundary also become steady with fluctuations, which includes combined effects of statistical particle noise and wave activities. In this work, we only focus on direct current (DC) electromagnetic fields. It would be more appropriate to leave the analysis of wave activities to future work with a 3-D simulation domain. Therefore, we averaged the electromagnetic fields over the last 20 s of the total simulation time (180–200 s in Figure 1). The results of electromagnetic field distributions are shown in Figure 2.

Figure 2a shows the original magnetic field (\mathbf{B}_0) of a crustal magnetic cusp, which stays constant through the simulation. The induced magnetic field (\mathbf{B}_1) as shown in Figure 2b is mostly pointing downward. The induced

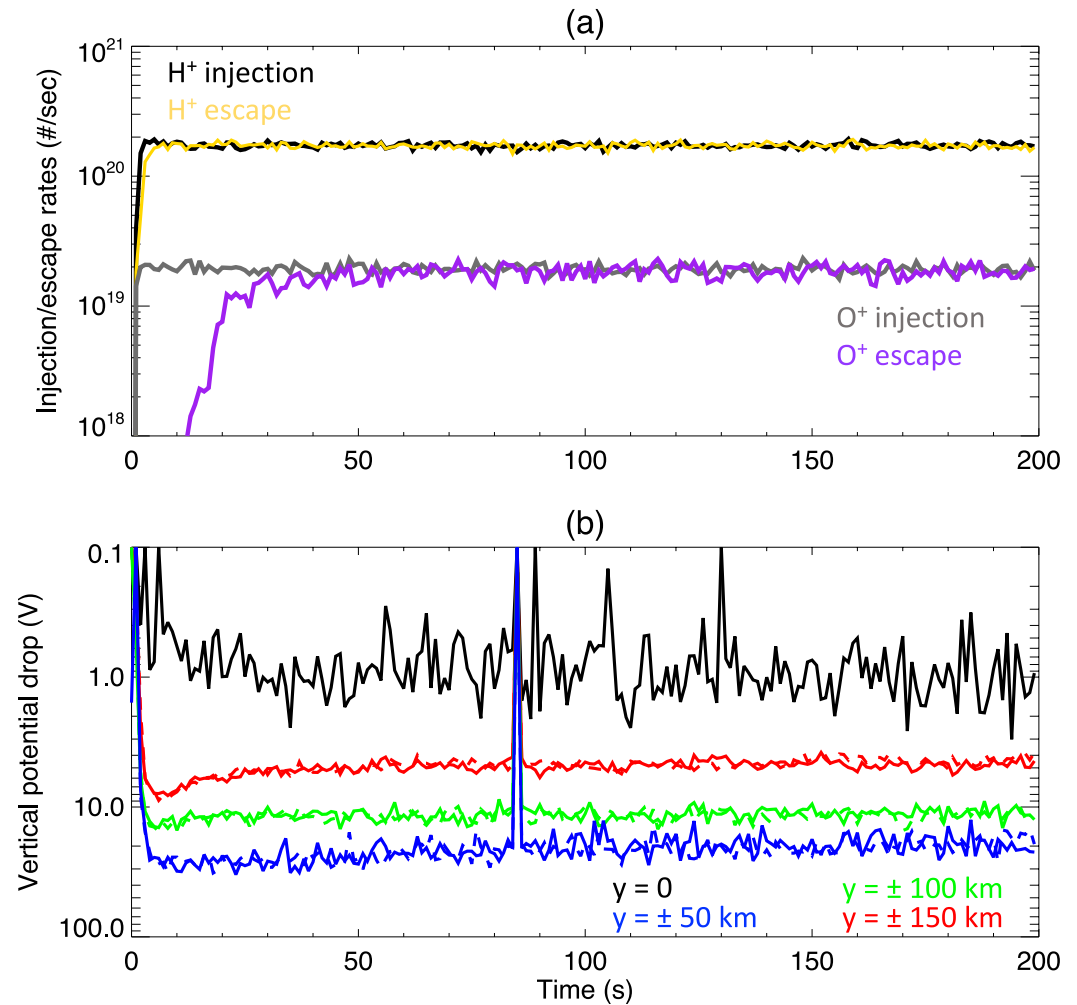


Figure 1. (a) Injection and escape rates for the two ion populations as a function of time from the model. (b) The vertical potential drop at different locations along the upper boundary. Dashed and solid lines correspond to negative and positive y coordinates, respectively.

magnetic field strength is much smaller than the crustal field. Thus it does not modify the original magnetic field significantly, as shown in Figure 2c. The convection ($-\mathbf{U}_i \times \mathbf{B}$) and Hall ($\mathbf{J} \times \mathbf{B}/(n_e e)$) terms of electric field in Equation 5 are shown in panels (d) and (e). These two terms of electric field are mostly in the opposite directions. The third term, ambipolar electric field ($-\nabla P_e/(n_e e)$) is not shown here because it is much smaller than the other two terms and the distribution does not show a clear pattern except that there are more cells with upward than downward ambipolar electric field presenting in the simulation domain. As shown in Figure 2f, the total electric field follows the pattern of the Hall term and is mostly pointing upward. The strength of the total electric field is 10^{-5} – 10^{-2} V/m in the simulation domain, which gives the O⁺ ions a much larger acceleration than the gravity near Mars' surface. Therefore, the effect of the lack of gravity in the model run is expected to be insignificant.

In Figure 3 we present the results of particle distributions and dynamics. Panels (a) and (b) show that the magnetospheric H⁺ ions injected from the upper boundary with a downward initial flow velocity of 100 km/s are significantly decelerated by the upward total electric field (see Figure 2f) and become denser in the central cusp region. The estimated gyroradius ($r_g = m_i v/(eB)$) for the H⁺ ions is a few tens of km in most of the simulation region with the velocity $v \sim 50$ – 100 km/s and magnetic field $B \sim 1$ – 100 nT as shown in Figures 2c and 3b, which means the Lorentz force from the magnetic field ($e\mathbf{v} \times \mathbf{B}$) would significantly deflect the H⁺ ions in the direction perpendicular to the $x - y$ plane. From Figure 3c it can be seen that the downward moving H⁺ ions are deflected by the magnetic field into the $x - y$ plane ($+z$ direction) on the $-y$ side and out of the $x - y$ plane ($-z$ direction) on the $+y$ side, which would form a clockwise loop of H⁺ ion flow in the horizontal plane in a 3-D domain with a

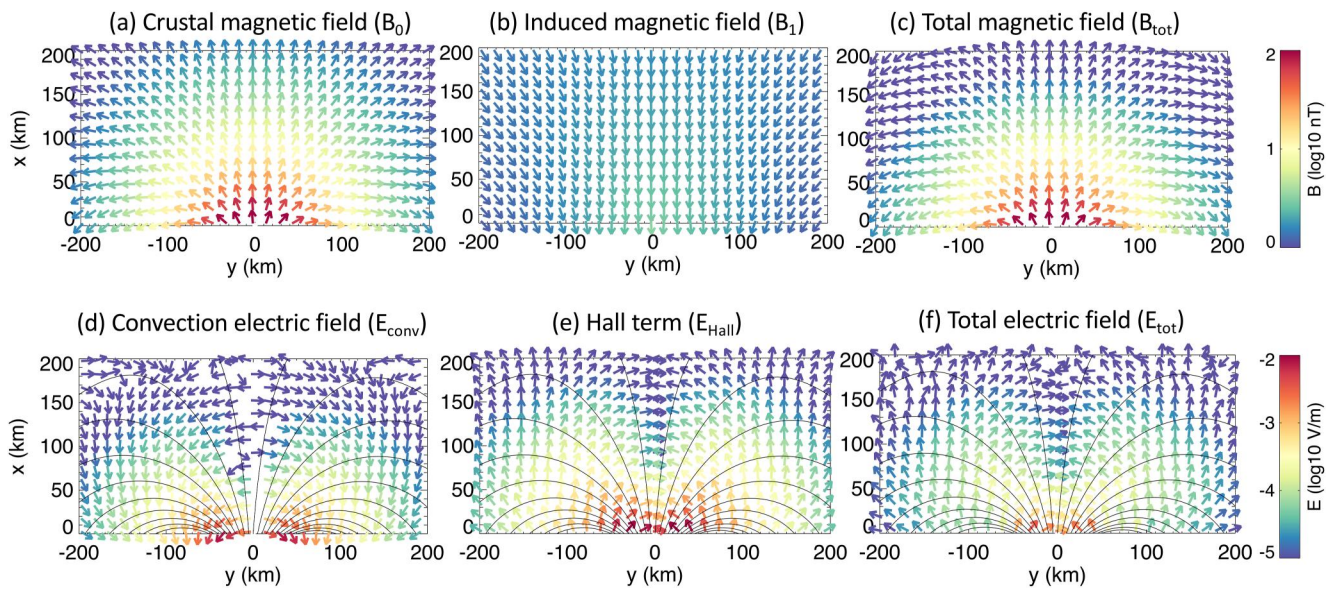


Figure 2. (a–c) Magnetic field distributions. (d–e) Electric field distributions superimposed on magnetic field lines.

cylindrically symmetric cusp field configuration. As shown in Figures 3d and 3e, the ionospheric O^+ ions injected from the lower boundary with an initial upward flow velocity of 1 km/s are accelerated to 10–20 km/s by the upward electric field, which leads to a significant density drop of O^+ in the central cusp region. The gyroradius for O^+ ions is estimated to be from a few tens of km to over 100 km in most of the simulation domain with the velocity $v \sim 5\text{--}10$ km/s and magnetic field $B \sim 1\text{--}100$ nT as shown in Figures 2c and 3e. Thus the upward moving O^+ ions are deflected by the magnetic field in opposite directions to the H^+ ions in the horizontal directions as shown in Figure 3f, which would form a counterclockwise ion flow loop in the horizontal plane. From Figure 1a, it can be seen that the magnetospheric H^+ injection rate is 10 times higher than the ionospheric O^+ injection rate. Consequently, the H^+ number flux dominates over the O^+ number flux in the simulation domain. Thus there is a net downward ion flow in the vertical plane and a net clockwise ion flow in the horizontal plane.

Figure 3h exhibits the acceleration of electron flow downward along the magnetic field lines as determined by Equation 3. As shown in Figure 3i, the horizontal electron flow is pointing into the $x - y$ plane ($+z$ direction) on the $-y$ side and out of the $x - y$ plane ($-z$ direction) on the $+y$ side (i.e., a counterclockwise loop in the horizontal plane), which is consistent with the $\mathbf{E} \times \mathbf{B}$ drift motion of electrons and a natural result considering the first two terms in Equation 5 can be written as $(-\mathbf{U}_e \times \mathbf{B})$. As shown in Figure 3j, the current directions are aligned with magnetic field lines in the central cusp region, which means the model at least qualitatively reproduced the field aligned currents. These upward field aligned currents will return to the lower boundary according to Figure 3j. By comparing the ion and electron fluxes from the model results, it can be told that these field-aligned currents are carried mostly by electrons and the returning currents are carried by the net downward ion flow.

Since the vertical electric field and potential drops are directly responsible for the acceleration of both precipitating and escaping particles, in Figure 4 we show the analysis of these two physical values from the model results. Figure 4a shows the spatial distribution of vertical electric field E_x , which is upward (positive) everywhere. Since the two major terms (convection and B and Hall terms) of electric field in Equation 5 are both perpendicular to the magnetic field, E_x is large in the region where there is a strong horizontal component of the magnetic field and very small near the vertical (x) axis where the magnetic field line is mostly vertical. Figure 4b shows the vertical potential drop distribution, which is calculated by integrating E_x from the lower boundary along the vertically upward ($+x$) direction (not along magnetic field lines). The region with large vertical potential drops in Figure 4b is consistent with the region where ionospheric O^+ ions are significantly accelerated in Figure 3e. From Figure 4c, it can be seen that the potential drop at the upper boundary is up to ~ 40 V (maximum found at $y \sim \pm 30\text{--}40$ km) and the averaged potential drop over the horizontal direction is ~ 12 V, both are significant potential drops for accelerating heavy ions at Mars considering the escape energy of O^+ is ~ 2 eV near Mars' surface. The contributions from different terms in Equation 5 to the average E_x are shown in Figure 4d. The

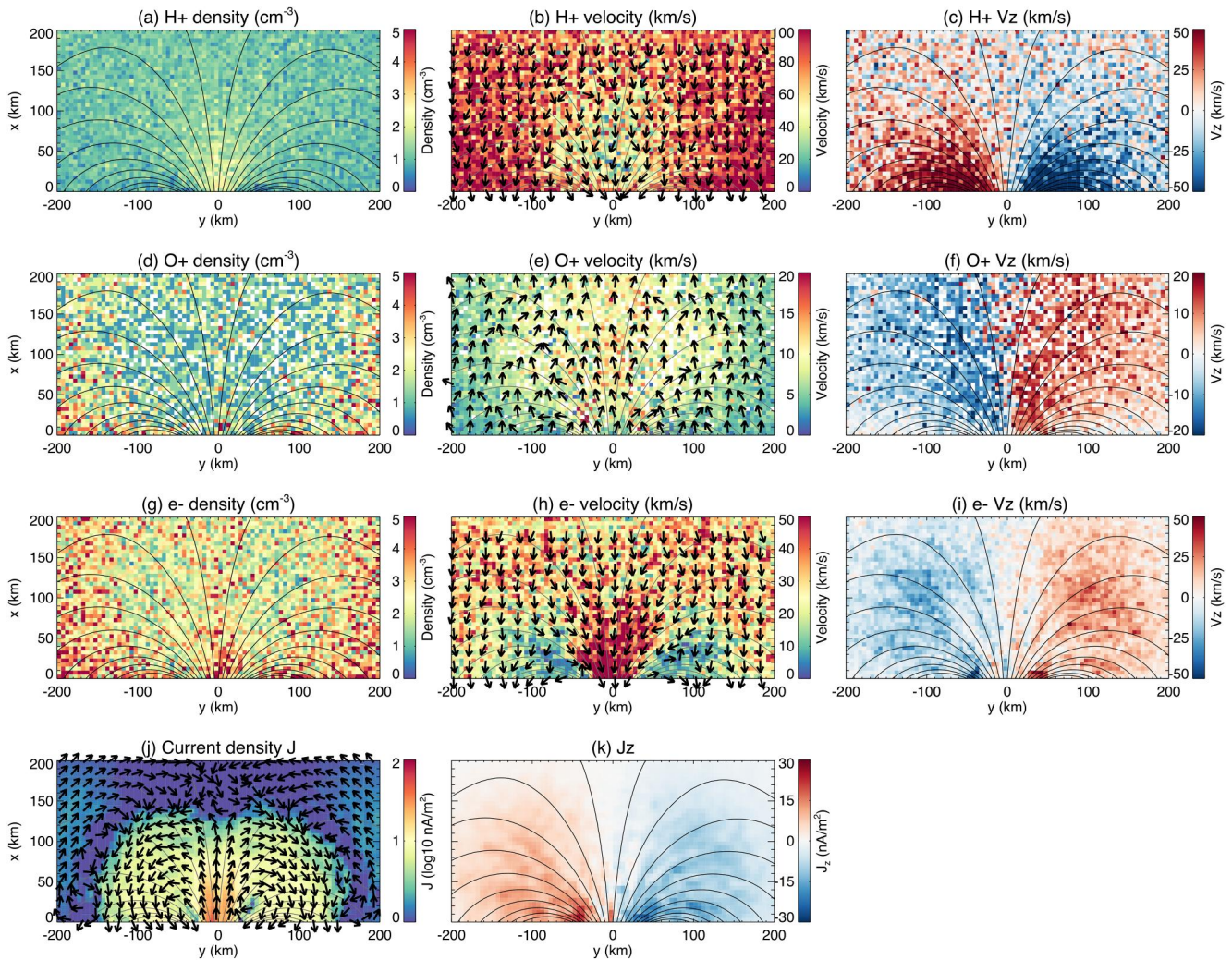


Figure 3. (a–i) Ion and electron density and velocity distributions. (j) and (k) Current density distributions.

Hall term ($\mathbf{J} \times \mathbf{B}/(n_e e)$) is the major contribution to the vertical potential drop. The convection term ($-\mathbf{U}_i \times \mathbf{B}$) is pointing downward, opposite to and smaller than the Hall term (see also Figures 2d and 2e). Although the ambipolar electric field is much smaller than the other two terms, it has a positive contribution to the vertical potential drop and is likely responsible for the acceleration of electrons along the magnetic field lines (see Figure 3h), since the other two terms are both perpendicular to the magnetic field. As mentioned in Section 2, the ambipolar electric field in the model run can only be considered as a rough estimate, which will be further discussed in Section 5.

4. Mechanism of the Vertical Potential Drop Buildup

From all the model results presented above, we can now understand how the system is built up. Figure 5 shows a simplified structure of the plasma flows, currents, and electromagnetic fields in the system. As mentioned in Section 3, the net downward ion flow is deflected clockwise in the horizontal plane by the magnetic field (Figure 5). As shown in Figure 2d, the clockwise horizontal ion flow and the horizontal magnetic field component result in a downward convection electric field. The electron flow moves in the opposite direction from the net ion flow in the horizontal plane as a result of $\mathbf{E} \times \mathbf{B}$ drift, which forms a clockwise current loop (Figure 5). This current loop induces a downward magnetic field (\mathbf{B}_1) as shown in Figure 2b. The clockwise current loop and the horizontal magnetic field component generate an upward Hall electric field, which

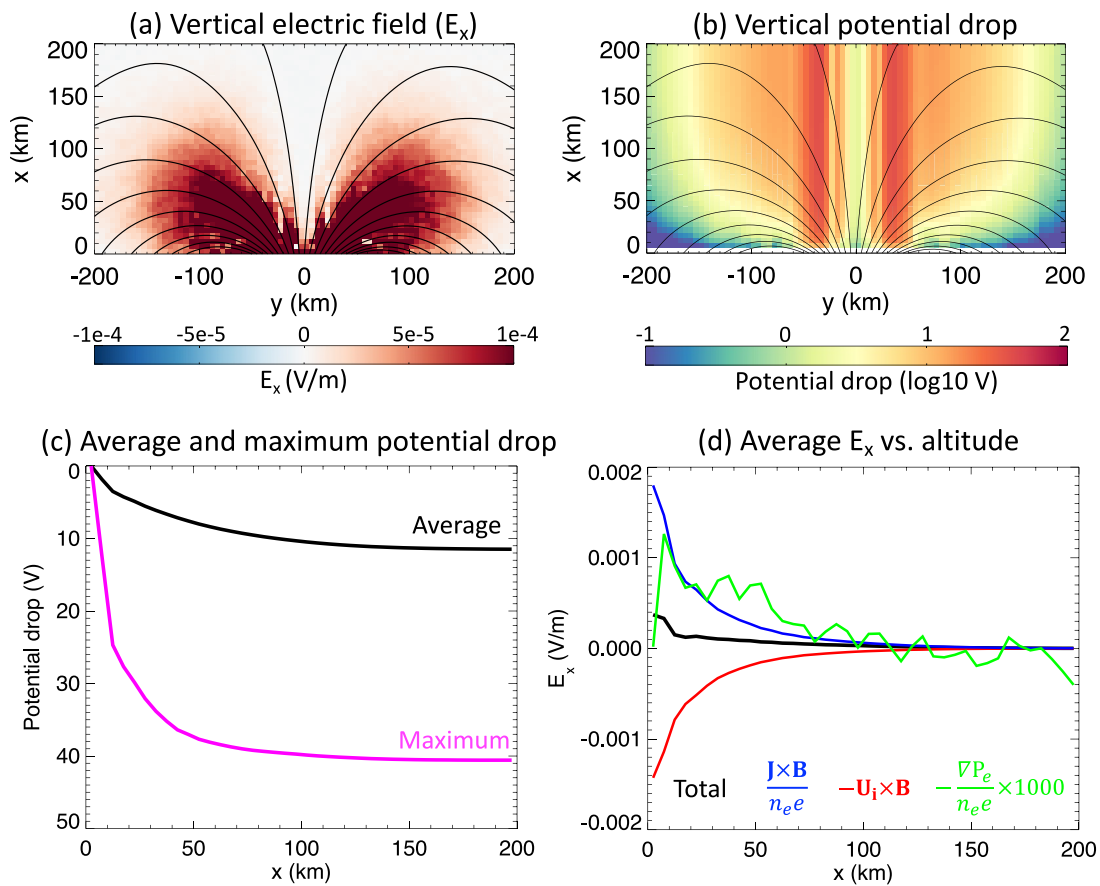


Figure 4. (a) and (b) Distributions of vertical electric field and potential drop (not along magnetic field lines). (c) Maximum and average potential drop over the horizontal direction as a function of the vertical distance from the lower boundary. (d) The different terms of the average vertical electric field as a function of the vertical distance from the lower boundary.

dominates over the downward convection electric field to produce a total upward electric field as shown in Figures 2d–2f, similar to the hybrid model results for lunar magnetic anomalies by Jarvinen et al. (2014). The horizontal current loop as a result of separation between electron and ion flows is the key for the buildup of the system and vertical potential drop.

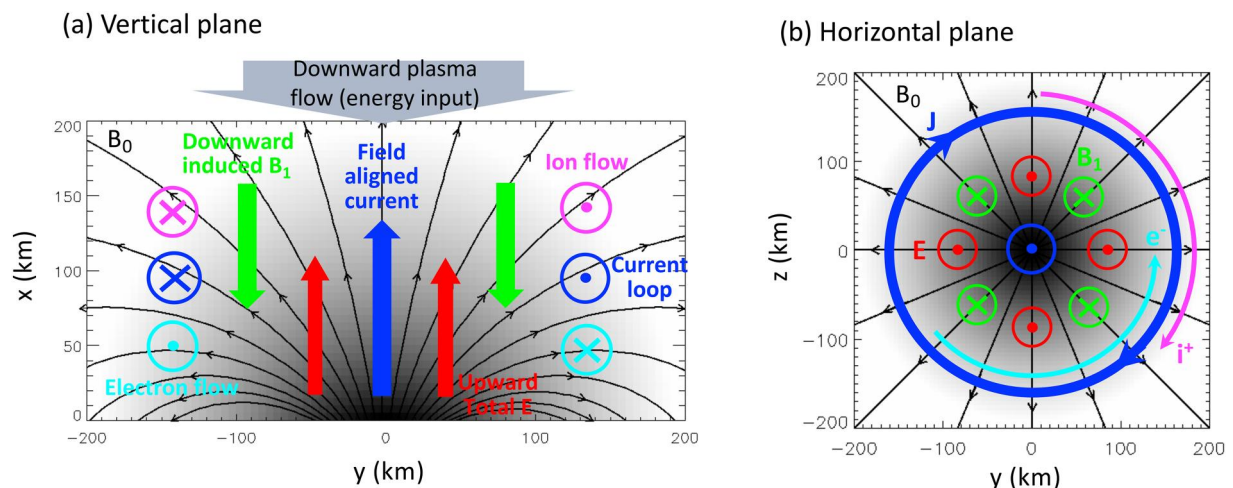


Figure 5. Simplified structures of ion and electron flows, currents, and electromagnetic fields in the system. Note that the cartoons do not show spatial distributions properly.

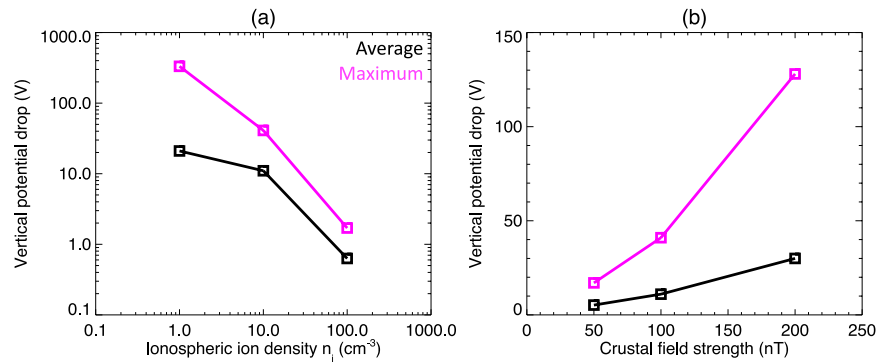


Figure 6. The average and maximum potential drop at the upper boundary as functions of different ionospheric ion densities and crustal field strengths.

As mentioned in Section 2, the 2-D simulation domain is actually equivalent to a 3-D domain with infinite distance in the third dimension instead of a cylindrically symmetric configuration as in Figure 5. With an infinite distance in the third dimension, the horizontal currents would form in opposite directions along the third dimension ($\pm z$) on each side of the magnetic cusp as shown in Figure 3k, which would build up a qualitatively identical system in the vertical plane as that in Figure 5a. Therefore, we consider the 2-D simulation domain to be a valid simplification for the 3-D cusp magnetic field configuration for studying the vertical electric potential structure and particle dynamics. Although the real Martian crustal magnetic cusps are more irregular shaped in the horizontal plane than that in Figure 5 (Connerney et al., 2005), a non-circular current loop may still form around the cusp to allow such a system to build up. We have also done a test run with the same model settings as in Table 1 except for reversed crustal field directions. Results from the test run (not shown here) exhibit reversed horizontal current and induced magnetic field, but the same electric field distribution and potential drop in the vertical plane, which tells us that polarity of the magnetic cusp does not affect the potential drop buildup.

More model runs have been done with different ionospheric O^+ densities (1 and 100 cm⁻³) and different crustal magnetic field strengths (50 and 100 nT). All the model results still show similar particle, current, and electromagnetic field distributions as those in Figures 2 and 3, which means the basic structure of the system as shown in Figure 5 does not vary with the changing parameters in this range. In Figure 6, we compare the maximum and average vertical potential drops at the upper boundary with ionospheric O^+ densities (n_i) and crustal magnetic field strengths (B_0). The trends are very clear: the vertical potential drop decreases with n_i but increases with B_0 . As shown in Figures 3b and 3e, the upward electric field accelerates ionospheric O^+ and decelerates magnetospheric H^+ . The buildup of the vertical potential drop represents the energy transfer between the two plasma populations. The injected magnetospheric plasma flow serves as an energy input to the system and an initial driver for vertical electric potential drop buildup. Through the upward electric field, energy is transferred from the decelerated magnetospheric H^+ to the accelerated ionospheric O^+ . When the energy input to the system is the same but the ionospheric O^+ density is increased, the same energy has to be shared among more ionospheric ions and each ion gets less acceleration, which explains why the potential drop decreases with n_i . The increase of the potential drop with crustal magnetic field strengths is also easily understandable. Since the convection and Hall terms Equation 5 can also be written together as $-\mathbf{U}_e \times \mathbf{B}$, stronger magnetic field would result in stronger upward electric field assuming \mathbf{U}_e does not change significantly. In other words, without any physical collisions between particles in the model, the magnetic cusp serves as a channel for the energy transfer between the two plasma populations, the efficiency of which increases with magnetic field strength.

5. Discussion

In this model, the convection and Hall electric fields, both perpendicular to the magnetic field, are much stronger than the ambipolar electric field, the only term in Equation 5 that can have a component parallel to the magnetic field and contributes to the field aligned potential drop. Poppe et al. (2021) simulated the field aligned potential drop in Martian crustal magnetic cusps using a fully kinetic PIC model. With a similar set of ionospheric and magnetospheric plasma and magnetic field parameters to those in this work, the potential drop from their PIC model falls in the range of tens of Volts, also similar to our results as shown in Figure 6. Besides, the trend that the

potential drop increases with crustal magnetic field strength is also consistent between the two models. PIC model solves the field aligned electric field self-consistently with both ion and electron dynamics. Thus the ambipolar electric field and the terms not included in Equation 5, such as the electron inertia term, are better represented in the PIC model. On the other hand, the two major electric field terms in our model: convection and Hall electric fields, which are both perpendicular to the magnetic field and related to horizontal ion and electron flows, are not well represented in the PIC model with only one spatial dimension along the magnetic field. Therefore, although Poppe et al. (2021)'s PIC model and our hybrid model result in similar potential drops in the magnetic cusp, the two models are actually complementary to each with different electric fields: parallel and perpendicular to the magnetic field respectively, which tells us that both field-aligned and perpendicular (to magnetic field) electric fields may be significant in the cusp region. Thus the crustal magnetic cusps may play an important role not only in the field aligned acceleration of electron precipitation (e.g., Xu et al., 2020) and ion outflow (e.g., Dubinin et al., 2009; Lundin et al., 2006), but also in the acceleration of unmagnetized ionospheric ions to move across magnetic field lines (Weber et al., 2021).

The ambipolar electric field is the only electric field in this model that can accelerate electrons along magnetic field lines. Figure 3b shows some field-aligned acceleration of electrons in the central cusp region by the ambipolar electric field. However, according to Figure 4d it is too small to explain the observed acceleration of precipitating electrons that cause discrete aurorae (Brain & Halekas, 2012; Dubinin et al., 2009; Halekas et al., 2008; Xu et al., 2020). Although the ambipolar electric field strength as shown in Figure 4d is generally consistent with the average ambipolar electric field in the ionosphere based on MAVEN data (Akbari et al., 2019; Collinson et al., 2019; Xu et al., 2018), we have to keep in mind that it is only a rough estimate with a manually set constant electron temperature and a simplified model setup without gravity (see Section 2). As shown by Poppe et al. (2021), with electron kinetics and gravitationally bound ionospheric ions in the model it is possible to get a much stronger field aligned electric field in the magnetic cusp than the average ionosphere ambipolar electric field. Besides, the energetic precipitating electrons may also be accelerated by the much stronger ambipolar electric field at higher altitudes (see Ma et al., 2019; Xu et al., 2021) or get energized from magnetic reconnections (see Harada et al., 2018; Ma et al., 2018). Although our localized model cannot reproduce a field-aligned potential drop large enough to cause discrete aurorae, the mechanism reported here may coincide with patchy proton aurorae (Chaffin et al., 2022) on Mars, since both may occur when there are incident proton fluxes to the ionosphere and atmosphere. We will leave the study of the connection with patchy proton aurorae to future work.

The vertical potential drop from the convection and Hall electric fields in this model accelerates ionospheric ions upward significantly. However, whether it enhances ion escape in the cusp region depends on other factors as well. In the model, the origin of the magnetospheric plasma is not specified. It can be incident solar wind plasma, returning planetary plasma, or a combination of both. Besides, the ion species does not have much influence on the mechanism of the potential drop build up. As shown in Section 2, both H^+ and heavy ions in the simulation domain would have a gyroradius that is large enough for them to be significantly deflected by magnetic field from the electron flow to form a current loop as shown in Figure 5. From Figure 6a it can be told that the more dominant the downward magnetospheric plasma flow is over the upward ionospheric plasma flow the larger the potential drop is, which means a sufficient net downward plasma flow is needed to build up a significant potential drop. Therefore, there can be three scenarios for whether this potential drop buildup mechanism actually enhances ion escape: **1)** If the downward magnetospheric plasma flow originates from solar wind, this process does enhance the escape of planetary ions in the magnetic cusp. **2)** If the downward magnetospheric plasma flow is composed of returning planetary ions of the same species as the ionospheric plasma, it does not enhance the ion escape because there is a net returning planetary ion flow of that species. **3)** If the downward magnetospheric plasma flow is composed of returning planetary ions of a different species from the ionospheric ions, it does enhance the escape of that certain ionospheric ion species. However, in real situation, both plasma populations may contain multiple ion species and origins, and thus, these three scenarios may co-exist, which would require case-to-case analysis to find out whether the ion escape is enhanced.

Our model simulates a steady state of the Martian magnetic cusp region with continuously injected ionospheric and magnetospheric plasma at constant rates without spatial variations such as incident waves. As discussed in the paragraph above, neither the origin nor the ion species for the incident magnetospheric plasma has much influence on the mechanism of the potential drop buildup in this model. The incident "magnetospheric" ions may be precipitating H^+ or O^+ (e.g., Dieval et al., 2013; Leblanc et al., 2015) on the dayside of Mars, and may be returning H^+ or heavy ions on the nightside (e.g., Harada et al., 2015). On the dayside, where the ionosphere has a

constant supply from photoionization (Withers, 2009 and references therein), during ion precipitating events a steady state of the magnetic cusp region as in our model may exist. Without precipitating ions, the potential drop would not build up to remove ionospheric ions. Either way, the ionospheric condition in the dayside cusp region may stay stable under the mechanism in this model. However, on the nightside, the ionospheric density is generally lower than the dayside and the supply (day-night plasma transport and ionization by precipitating particle impacts) is less steady (e.g., Adams et al., 2018; Withers et al., 2012). The dependence of vertical potential drop on ionosphere density as shown in Figure 6a suggests that without a constant and sufficient supply to the ionosphere, the increase of potential drop with the decrease of ionosphere density would work as a positive feedback loop, which may result in removing ionospheric ions quickly and breaking the steady state. Thus during ion precipitating events in a nightside cusp region, the ionosphere may be unstable, which might contribute to the variability of Mars' nightside ionosphere (Girazian et al., 2017). Dubinin et al. (2008) also suggested a non-steady state of the cusp region when the field-aligned current cannot be closed in the ionosphere. Since the hybrid model assumes quasi-neutrality and all currents can go freely out of the simulation domain, it will automatically lead to closed current systems. Thus the scenario in Dubinin et al. (2008) cannot be reproduced in our model. A non-steady state of the crustal magnetic cusp region is plausible in real situation, which will be an interesting topic for future study.

In this work, we use a 2-D simulation domain for efficiency and to focus on the vertical electric potential structure. However, as discussed in Section 4, the horizontal plasma flows are crucial for building up the vertical electric potential drop. Some previous works based on observations and simulations have also found ion flow being deflected in the horizontal plane near strong crustal fields (e.g., Fan et al., 2020; Li et al., 2022). For future work, it would be interesting to do a comparison with the observed ion flows near cusp regions with a 3-D simulation domain and more realistic plasma parameter settings. Our model simulates a region within 200 km above the exobase, which only provides a local mechanism for the potential drop buildup. To fully understand the electric potential structure and particle dynamics in the cusp region, other electric fields and acceleration processes below the exobase in the dynamo region (RiOUSSET et al., 2013, 2014) and at higher altitudes (Harada et al., 2018; Kallio et al., 2008; Ma et al., 2018, 2019; Xu et al., 2021) should also be taken into consideration.

6. Summary

We have applied the quasi-neutral ion-kinetic hybrid simulation platform HYB to a 2-D simulation domain with a moderately strong magnetic cusp above the exobase and two plasma populations: magnetospheric and ionospheric plasma injected from the upper and lower boundaries respectively. The hybrid model can qualitatively reproduce the vertical electric potential drop and field aligned currents in the central cusp region. The potential drop is mostly from the Hall electric field as a result of the separation between ion and electron flows in the horizontal plane. The field aligned currents are carried by downward electron flows accelerated by the ambipolar electric field. The model results with different ionospheric ion densities and crustal field strengths as input show that the vertical potential drop decreases with ionospheric ion densities and increases with crustal field strengths.

These results tell us: **1)** The magnetic cusp serves as a channel for the energy exchange between the two plasma populations, for which the efficiency is higher with stronger magnetic field. **2)** The incident magnetospheric plasma, which may have planetary or solar wind origination, is the energy input to the system, and a dominant downward plasma flow is necessary for a significant potential drop to build up. **3)** Although the vertical electric potential drop accelerates ionospheric ions, whether this mechanism in the model enhances ion escape in the cusp region depends on the origin and ion species of the incident magnetospheric plasma. **4)** The nightside ionosphere in the cusp region during ion precipitating events without a sufficient and continuous supply may be unstable under this mechanism, since the decrease of ionosphere density and the increase of electric potential drop will form a positive feedback loop.

Data Availability Statement

Simulations were performed using the HYB code distributed under the open source GPL v3 license by the Finnish Meteorological Institute (github.com/fmihpc/hyb). The simulation code version used in this study is archived (<https://doi.org/10.5281/zenodo.10517964>).

Acknowledgments

This work was supported by NASA’s Solar System Workings program through grant NNX16AR94G and NASA MAVEN project through the Mars Exploration Program. This work utilized the Summit and Alpine high performance computing resources at the University of Colorado Boulder. The Summit supercomputer is supported by the National Science Foundation (awards ACI-1532235 and ACI-1532236), the University of Colorado Boulder, and Colorado State University. Alpine is jointly funded by the University of Colorado Boulder, the University of Colorado Anschutz, and Colorado State University. The authors would like to thank Dr. Hilary Egan for her help with the use of the high performance computing resources.

References

Acuña, M., Connerney, J., Ness, Lin, R., Mitchell, D., Carlson, C., et al. (1999). Global distribution of crustal magnetization discovered by the Mars Global Surveyor MAG/ER experiment. *Science*, 284(5415), 790–793. <https://doi.org/10.1126/science.284.5415.790>

Acuña, M., Connerney, J., Wasilewski, P. a., Lin, R., Anderson, K., Carlson, C., et al. (1998). Magnetic field and plasma observations at Mars: Initial results of the Mars Global Surveyor mission. *Science*, 279(5357), 1676–1680. <https://doi.org/10.1126/science.279.5357.1676>

Adams, D., Xu, S., Mitchell, D., Lillis, R., Fillingim, M., Andersson, L., et al. (2018). Using magnetic topology to probe the sources of Mars’ nightside ionosphere. *Geophysical Research Letters*, 45(22), 12–190. <https://doi.org/10.1029/2018gl080629>

Akbari, H., Andersson, L., Peterson, W., Espley, J., Benna, M., & Ergun, R. (2019). Ambipolar electric field in the Martian ionosphere: MAVEN measurements. *Journal of Geophysical Research: Space Physics*, 124(6), 4518–4524. <https://doi.org/10.1029/2018ja026325>

Alho, M. (2016). Hybrid plasma modelling of lunar magnetic anomalies.

Andrews, D., Edberg, N. J., Eriksson, A. I., Gurnett, D., Morgan, D., Němec, F., & Opgenoorth, H. J. (2015). Control of the topside Martian ionosphere by crustal magnetic fields. *Journal of Geophysical Research: Space Physics*, 120(4), 3042–3058. <https://doi.org/10.1002/2014ja020703>

Axford, W. (1968). The polar wind and the terrestrial helium budget. *Journal of Geophysical Research*, 73(21), 6855–6859. <https://doi.org/10.1029/ja073i021p06855>

Bertaux, J.-L., Leblanc, F., Witasse, O., Quémenerais, E., Liliensten, J., Stern, S., et al. (2005). Discovery of an aurora on Mars. *Nature*, 435(7043), 790–794. <https://doi.org/10.1038/nature03603>

Brain, D. A., Bagenal, F., Acuña, M. H., & Connerney, J. E. P. (2003). Martian magnetic morphology: Contributions from the solar wind and crust. *Journal of Geophysical Research: Space Physics*, 108(A12), 1024. <https://doi.org/10.1029/2002JA009482>

Brain, D. A., Baker, A., Briggs, J., Eastwood, J., Halekas, J., & Phan, T.-D. (2010). Episodic detachment of Martian crustal magnetic fields leading to bulk atmospheric plasma escape. *Geophysical Research Letters*, 37(14), L14108. <https://doi.org/10.1029/2010gl043916>

Brain, D. A., Halekas, J., Lillis, R., Mitchell, D., Lin, R., & Crider, D. (2005). Variability of the altitude of the Martian sheath. *Geophysical Research Letters*, 32(18), L18203. <https://doi.org/10.1029/2005gl023126>

Brain, D. A., Halekas, J., Peticolas, L., Lin, R., Luhmann, J., Mitchell, D., et al. (2006). On the origin of aurorae on Mars. *Geophysical Research Letters*, 33(1), L01201. <https://doi.org/10.1029/2005gl024782>

Brain, D. A., & Halekas, J. S. (2012). Aurora in Martian mini magnetospheres. *Auroral Phenomenology and Magnetospheric Processes: Earth and Other Planets*, 197, 123–132.

Brecht, S. H., & Ledvina, S. A. (2014). The role of the Martian crustal magnetic fields in controlling ionospheric loss. *Geophysical Research Letters*, 41(15), 5340–5346. <https://doi.org/10.1002/2014gl060841>

Chaffin, M. S., Fowler, C. M., Deighan, J., Jain, S., Holsclaw, G., Hughes, A., et al. (2022). Patchy proton aurora at Mars: A global view of solar wind precipitation across the Martian dayside from EMM/EMUS. *Geophysical Research Letters*, 49(17), e2022GL099881. <https://doi.org/10.1029/2022gl099881>

Chicarro, A., Martin, P., & Trautner, R. (2004). *The Mars express mission: An overview*. In *Mars Express: The Scientific Payload*. Ed. by Andrew Wilson, Scientific Coordination: Agustin Chicarro. ESA SP-1240 (pp. 3–13). ESA Publications Division. ISBN 92-9092-556-6, 1240.

Collinson, G., Glocer, A., Xu, S., Mitchell, D., Frahm, R. A., Grebowsky, J., et al. (2019). Ionospheric ambipolar electric fields of Mars and Venus: Comparisons between theoretical predictions and direct observations of the electric potential drop. *Geophysical Research Letters*, 46(3), 1168–1176. <https://doi.org/10.1029/2018gl080597>

Connerney, J., Acuña, M., Ness, N., Kletetschka, G., Mitchell, D., Lin, R., & Reme, H. (2005). Tectonic implications of Mars crustal magnetism. *Proceedings of the National Academy of Sciences*, 102(42), 14970–14975. <https://doi.org/10.1073/pnas.0507469102>

Deighan, J., Jain, S., Chaffin, M., Fang, X., Halekas, J. S., Clarke, J. T., et al. (2018). Discovery of a proton aurora at Mars. *Nature Astronomy*, 2(10), 802–807. <https://doi.org/10.1038/s41550-018-0538-5>

Dieval, C., Stenberg, G., Nilsson, H., & Barabash, S. (2013). A statistical study of proton precipitation onto the Martian upper atmosphere: Mars express observations. *Journal of Geophysical Research: Space Physics*, 118(5), 1972–1983. <https://doi.org/10.1002/jgra.50229>

Dong, Y., Brain, D., Ramstad, R., Fang, X., McFadden, J., Halekas, J., et al. (2023). The dependence of Martian ion escape on solar euv irradiance as observed by MAVEN. *Icarus*, 393, 115288. <https://doi.org/10.1016/j.icarus.2022.115288>

Dong, Y., Fang, X., Brain, D., Hurley, D., Halekas, J., Espley, J., et al. (2019). Magnetic field in the Martian magnetosheath and the application as an IMF clock angle proxy. *Journal of Geophysical Research: Space Physics*, 124(6), 4295–4313. <https://doi.org/10.1029/2019ja026522>

Dubinin, E., Chanteur, G., Fraenz, M., & Woch, J. (2008). Field-aligned currents and parallel electric field potential drops at Mars: scaling from the earth’ aurora. *Planetary and Space Science*, 56(6), 868–872. <https://doi.org/10.1016/j.pss.2007.01.019>

Dubinin, E., Fraenz, M., Andrews, D., & Morgan, D. (2016). Martian ionosphere observed by Mars express. 1. Influence of the crustal magnetic fields. *Planetary and Space Science*, 124, 62–75. <https://doi.org/10.1016/j.pss.2016.02.004>

Dubinin, E., Fraenz, M., Woch, J., Barabash, S., & Lundin, R. (2009). Long-lived auroral structures and atmospheric losses through auroral flux tubes on Mars. *Geophysical Research Letters*, 36(8), L08108. <https://doi.org/10.1029/2009gl038209>

Edberg, N., Lester, M., Cowley, S., & Eriksson, A. (2008). Statistical analysis of the location of the Martian magnetic pileup boundary and bow shock and the influence of crustal magnetic fields. *Journal of Geophysical Research*, 113(A8), A08206. <https://doi.org/10.1029/2008ja013096>

Ergun, R., Andersson, L., Fowler, C., Thaller, S., & Yelle, R. (2021). In-situ measurements of electron temperature and density in Mars’ dayside ionosphere. *Geophysical Research Letters*, 48(14), e2021GL093623. <https://doi.org/10.1029/2021gl093623>

Fan, K., Fraenz, M., Wei, Y., Cui, J., Rong, Z., Chai, L., & Dubinin, E. (2020). Deflection of global ion flow by the Martian crustal magnetic fields. *The Astrophysical Journal Letters*, 898(2), L54. <https://doi.org/10.3847/2041-8213/aba519>

Fang, X., Ma, Y., Brain, D., Dong, Y., & Lillis, R. (2015). Control of Mars global atmospheric loss by the continuous rotation of the crustal magnetic field: A time-dependent MHD study. *Journal of Geophysical Research: Space Physics*, 120(12), 10–926. <https://doi.org/10.1002/2015ja021605>

Fang, X., Ma, Y., Masunaga, K., Dong, Y., Brain, D., Halekas, J., et al. (2017). The Mars crustal magnetic field control of plasma boundary locations and atmospheric loss: MHD prediction and comparison with MAVEN. *Journal of Geophysical Research: Space Physics*, 122(4), 4117–4137. <https://doi.org/10.1002/2016JA023509>

Gérard, J.-C., Soret, L., Libert, L., Lundin, R., Stepen, A., Radioti, A., & Bertaux, J.-L. (2015). Concurrent observations of ultraviolet aurora and energetic electron precipitation with Mars express. *Journal of Geophysical Research: Space Physics*, 120(8), 6749–6765. <https://doi.org/10.1002/2015ja021150>

Girazian, Z., Mahaffy, P., Lillis, R., Benna, M., Elrod, M., & Jakosky, B. (2017). Nightside ionosphere of Mars: Composition, vertical structure, and variability. *Journal of Geophysical Research: Space Physics*, 122(4), 4712–4725. <https://doi.org/10.1002/2016ja023508>

- Halekas, J., Brain, D., Lin, R., Luhmann, J., & Mitchell, D. (2008). Distribution and variability of accelerated electrons at Mars. *Advances in Space Research*, 41(9), 1347–1352. <https://doi.org/10.1016/j.asr.2007.01.034>
- Harada, Y., Halekas, J., DiBraccio, G., Xu, S., Espley, J., McFadden, J., et al. (2018). Magnetic reconnection on dayside crustal magnetic fields at Mars: MAVEN observations. *Geophysical Research Letters*, 45(10), 4550–4558. <https://doi.org/10.1002/2018gl077281>
- Harada, Y., Halekas, J., McFadden, J., Mitchell, D., Mazelle, C., Connerney, J., et al. (2015). Marsward and tailward ions in the near-Mars magnetotail: MAVEN observations. *Geophysical Research Letters*, 42(21), 8925–8932. <https://doi.org/10.1002/2015gl065005>
- Heikkilä, W. J., & Winningham, J. (1971). Penetration of magnetosheath plasma to low altitudes through the dayside magnetospheric cusps. *Journal of Geophysical Research*, 76(4), 883–891. <https://doi.org/10.1029/ja076i004p00883>
- Iijima, T., & Potemra, T. A. (1976). Field-aligned currents in the dayside cusp observed by Triad. *Journal of Geophysical Research*, 81(34), 5971–5979. <https://doi.org/10.1029/ja081i034p05971>
- Inui, S., Seki, K., Namekawa, T., Sakai, S., Brain, D., Hara, T., et al. (2018). Cold dense ion outflow observed in the Martian-induced magnetotail by MAVEN. *Geophysical Research Letters*, 45(11), 5283–5289. <https://doi.org/10.1029/2018gl077584>
- Jakosky, B. M., Brain, D., Chaffin, M., Curry, S., Deighan, J., Grebowsky, J., et al. (2018). Loss of the Martian atmosphere to space: Present-day loss rates determined from MAVEN observations and integrated loss through time. *Icarus*, 315, 146–157. <https://doi.org/10.1016/j.icarus.2018.05.030>
- Jakosky, B. M., Lin, R. P., Grebowsky, J. M., Luhmann, J. G., Mitchell, D., Beutelschies, G., et al. (2015). The Mars atmosphere and volatile evolution (MAVEN) mission. *Space Science Reviews*, 195(1–4), 3–48. <https://doi.org/10.1007/s11214-015-0139-x>
- Jarvinen, R., Alho, M., Kallio, E., Wurz, P., Barabash, S., & Futaana, Y. (2014). On vertical electric fields at lunar magnetic anomalies. *Geophysical Research Letters*, 41(7), 2243–2249. <https://doi.org/10.1002/2014GL059788>
- Jarvinen, R., Brain, D. A., Modolo, R., Fedorov, A., & Holmström, M. (2018). Oxygen ion energization at Mars: Comparison of MAVEN and Mars express observations to global hybrid simulation. *Journal of Geophysical Research: Space Physics*, 123(2), 1678–1689. <https://doi.org/10.1002/2017ja024884>
- Jarvinen, R., Kallio, E., Dyadechkin, S., Janhunen, P., & Sillanpää, I. (2010). Widely different characteristics of oxygen and hydrogen ion escape from Venus. *Geophysical Research Letters*, 37(16), L16201. <https://doi.org/10.1029/2010gl044062>
- Kallio, E., Frahm, R., Futaana, Y., Fedorov, A., & Janhunen, P. (2008). Morphology of the magnetic field near Mars and the role of the magnetic crustal anomalies: Dayside region. *Planetary and Space Science*, 56(6), 852–855. <https://doi.org/10.1016/j.pss.2007.12.002>
- Kallio, E., Liu, K., Jarvinen, R., Pohjola, V., & Janhunen, P. (2010). Oxygen ion escape at Mars in a hybrid model: High energy and low energy ions. *Icarus*, 206(1), 152–163. <https://doi.org/10.1016/j.icarus.2009.05.015>
- Leblanc, F., Modolo, R., Curry, S., Luhmann, J., Lillis, R., Chaufray, J.-Y., et al. (2015). Mars heavy ion precipitating flux as measured by Mars atmosphere and volatile evolution. *Geophysical Research Letters*, 42(21), 9135–9141. <https://doi.org/10.1002/2015gl066170>
- Leblanc, F., Witasse, O., Liliensten, J., Frahm, R., Safaenili, A., Brain, D., et al. (2008). Observations of aurorae by SPICAM ultraviolet spectrograph on board Mars express: Simultaneous ASPERA-3 and Marsis measurements. *Journal of Geophysical Research: Space Physics*, 113(A8), A08311. <https://doi.org/10.1029/2008ja013033>
- Leblanc, F., Witasse, O., Winningham, J., Brain, D., Liliensten, J., Brelly, P.-L., et al. (2006). Origins of the Martian aurora observed by spectroscopy for investigation of characteristics of the atmosphere of Mars (SPICAM) on board Mars express. *Journal of Geophysical Research: Space Physics*, 111(A9). <https://doi.org/10.1029/2006ja011763>
- Li, S., Lu, H., Cao, J., Cui, J., Zhou, C., Wild, J. A., et al. (2022). Deflection of O₂⁺ ion flow by magnetic fields in the Martian ionosphere. *The Astrophysical Journal*, 941(2), 198. <https://doi.org/10.3847/1538-4357/aca32b>
- Lundin, R., Winningham, D., Barabash, S., Frahm, R., Holmstrom, M., Sauvaud, J.-A., et al. (2006). Plasma acceleration above Martian magnetic anomalies. *Science*, 311(5763), 980–983. <https://doi.org/10.1126/science.1122071>
- Ma, Y., Dong, C., Toth, G., Van der Holst, B., Nagy, A., Russell, C., et al. (2019). Importance of ambipolar electric field in driving ion loss from Mars: Results from a multifluid MHD model with the electron pressure equation included. *Journal of Geophysical Research: Space Physics*, 124(11), 9040–9057. <https://doi.org/10.1029/2019ja027091>
- Ma, Y., Fang, X., Russell, C. T., Nagy, A. F., Toth, G., Luhmann, J. G., et al. (2014). Effects of crustal field rotation on the solar wind plasma interaction with Mars. *Geophysical Research Letters*, 41(19), 6563–6569. <https://doi.org/10.1002/2014gl060785>
- Ma, Y., Nagy, A. F., Hansen, K. C., DeZeeuw, D. L., Gombosi, T. I., & Powell, K. (2002). Three-dimensional multispecies MHD studies of the solar wind interaction with Mars in the presence of crustal fields. *Journal of Geophysical Research: Space Physics*, 107(A10), 1282. <https://doi.org/10.1029/2002ja009293>
- Ma, Y., Russell, C. T., Toth, G., Chen, Y., Nagy, A. F., Harada, Y., et al. (2018). Reconnection in the Martian magnetotail: Hall-MHD with embedded particle-in-cell simulations. *Journal of Geophysical Research: Space Physics*, 123(5), 3742–3763. <https://doi.org/10.1029/2017JA024729>
- Mitchell, D., Lin, R., Mazelle, C., Rème, H., Cloutier, P., Connerney, J., et al. (2001). Probing Mars' crustal magnetic field and ionosphere with the mgs electron reflectometer. *Journal of Geophysical Research*, 106(E10), 23419–23427. <https://doi.org/10.1029/2000je001435>
- Mittelholz, A., Johnson, C., Feinberg, J., Langlais, B., & Phillips, R. (2020). Timing of the Martian dynamo: New constraints for a core field 4.5 and 3.7 Ga ago. *Science Advances*, 6(18), eaba0513. <https://doi.org/10.1126/sciadv.aba0513>
- Nilsson, H., Edberg, N. J., Stenberg, G., Barabash, S., Holmström, M., Futaana, Y., et al. (2011). Heavy ion escape from Mars, influence from solar wind conditions and crustal magnetic fields. *Icarus*, 215(2), 475–484. <https://doi.org/10.1016/j.icarus.2011.08.003>
- Poppe, A. R., Brain, D. A., Dong, Y., Xu, S., & Jarvinen, R. (2021). Particle-in-cell modeling of Martian magnetic cusps and their role in enhancing nightside ionospheric ion escape. *Geophysical Research Letters*, 48(1), e2020GL090763. <https://doi.org/10.1029/2020gl090763>
- Ramstad, R., Barabash, S., Futaana, Y., Nilsson, H., & Holmström, M. (2016). Effects of the crustal magnetic fields on the Martian atmospheric ion escape rate. *Geophysical Research Letters*, 43(20), 10–574. <https://doi.org/10.1002/2016gl070135>
- Ramstad, R., Barabash, S., Futaana, Y., Nilsson, H., Wang, X.-D., & Holmström, M. (2015). The Martian atmospheric ion escape rate dependence on solar wind and solar euv conditions: 1. Seven years of Mars express observations. *Journal of Geophysical Research: Planets*, 120(7), 1298–1309. <https://doi.org/10.1002/2015je004816>
- Rioux, J. A., Paty, C. S., Lillis, R. J., Fillingim, M. O., England, S. L., Withers, P. G., & Hale, J. P. (2014). Electrodynamics of the Martian dynamo region near magnetic cusps and loops. *Geophysical Research Letters*, 41(4), 1119–1125. <https://doi.org/10.1002/2013gl059130>
- Rioux, J. A., Paty, C. S., Lillis, R. J., Fillingim, M. O., England, S. L., Withers, P. G., & Hale, J. P. (2013). Three-dimensional multifluid modeling of atmospheric electrodynamics in Mars' dynamo region. *Journal of Geophysical Research: Space Physics*, 118(6), 3647–3659. <https://doi.org/10.1002/jgra.50328>
- Ritter, B., Gérard, J.-C., Hubert, B., Rodriguez, L., & Montmessin, F. (2018). Observations of the proton aurora on Mars with SPICAM on board Mars express. *Geophysical Research Letters*, 45(2), 612–619. <https://doi.org/10.1002/2017gl076235>

- Schneider, N., Deighan, J. I., Jain, S. K., Stiepen, A., Stewart, A. I. F., Larson, D., et al. (2015). Discovery of diffuse aurora on Mars. *Science*, 350(6261), aad0313. <https://doi.org/10.1126/science.aad0313>
- Schneider, N., Milby, Z., Jain, S., Gérard, J.-C., Soret, L., Brain, D., et al. (2021). Discrete aurora on Mars: Insights into their distribution and activity from MAVEN/IUVS observations. *Journal of Geophysical Research: Space Physics*, 126(10), e2021JA029428. <https://doi.org/10.1029/2021ja029428>
- Smith, M., & Lockwood, M. (1996). Earth's magnetospheric cusps. *Reviews of Geophysics*, 34(2), 233–260. <https://doi.org/10.1029/96rg00893>
- Tóth, G., Chen, Y., Gombosi, T. I., Cassak, P., Markidis, S., & Peng, I. B. (2017). Scaling the ion inertial length and its implications for modeling reconnection in global simulations. *Journal of Geophysical Research: Space Physics*, 122(10), 10–336. <https://doi.org/10.1002/2017ja024189>
- Weber, T., Brain, D., Xu, S., Mitchell, D., Espley, J., Mazelle, C., et al. (2021). Martian crustal field influence on O⁺ and O₂⁺ escape as measured by MAVEN. *Journal of Geophysical Research: Space Physics*, 126(8), e2021JA029234. <https://doi.org/10.1029/2021ja029234>
- Withers, P. (2009). A review of observed variability in the dayside ionosphere of Mars. *Advances in Space Research*, 44(3), 277–307. <https://doi.org/10.1016/j.asr.2009.04.027>
- Withers, P., Fillingim, M., Lillis, R., Häusler, B., Hinson, D., Tyler, G., et al. (2012). Observations of the nightside ionosphere of Mars by the Mars express radio science experiment (Mars). *Journal of Geophysical Research: Space Physics*, 117(A12), A12307. <https://doi.org/10.1029/2012ja018185>
- Xu, S., Liemohn, M. W., & Mitchell, D. L. (2014). Solar wind electron precipitation into the dayside Martian upper atmosphere through the cusps of strong crustal fields. *Journal of Geophysical Research: Space Physics*, 119(12), 10–100. <https://doi.org/10.1002/2014ja020363>
- Xu, S., Mitchell, D. L., Ma, Y., Weber, T., Brain, D. A., Halekas, J., et al. (2021). Global ambipolar potentials and electric fields at Mars inferred from MAVEN observations. *Journal of Geophysical Research: Space Physics*, 126(12), e2021JA029764. <https://doi.org/10.1029/2021ja029764>
- Xu, S., Mitchell, D. L., McFadden, J. P., Collinson, G., Harada, Y., Lillis, R., et al. (2018). Field-aligned potentials at Mars from MAVEN observations. *Geophysical Research Letters*, 45(19), 10–119. <https://doi.org/10.1029/2018gl080136>
- Xu, S., Mitchell, D. L., McFadden, J. P., Fillingim, M. O., Andersson, L., Brain, D. A., et al. (2020). Inverted-v electron acceleration events occurring with localized auroral observations at Mars by MAVEN. *Geophysical Research Letters*, 47(9), e2020GL087414. <https://doi.org/10.1029/2020gl087414>